Palaeogeography, Palaeoclimatology, Palaeoecology 346-347 (2012) 1–11

Contents lists available at SciVerse ScienceDirect

Palaeogeography, Palaeoclimatology, Palaeoecology

journal homepage: www.elsevier.com/locate/palaeo

Geochronological constraints on post-extinction recovery of the ammonoids and carbon cycle perturbations during the Early Jurassic

Jean Guex [a,*], Blair Schoene [b], Annachiara Bartolini [c], Jorge Spangenberg [d], Urs Schaltegger [e], Luis O'Dogherty [f], David Taylor [g], Hugo Bucher [h], Viorel Atudorei [i]

[a] Institute of Geology, Anthropole, University of Lausanne, Switzerland
[b] Department of Geosciences, 219 Guyot Hall, Princeton University, Princeton, NJ 08544, USA
[c] Museum d'Histoire Naturelle, Paris, France
[d] Institute of Geochemistry, Anthropole, University of Lausanne, Switzerland
[e] Earth and Environmental Sciences, University of Geneva, rue des Maraîchers 13, 1205, Geneva, Switzerland
[f] Dpto. Ciencias de la Tierra, Puerto Real, Spain
[g] North West Museum, 5004 Lowell, Portland, OR, USA
[h] Paleontologisches Institut, Universität Zürich, Switzerland
[i] Department of Geochemistry, University of New Mexico, Albuquerque, NM, USA

ARTICLE INFO

Article history:
Received 10 July 2011
Received in revised form 3 April 2012
Accepted 26 April 2012
Available online 5 May 2012

Keywords:
U–Pb dating
Carbon isotope stratigraphy
Triassic–Jurassic boundary
Peru
Mass extinction
Post extinction recovery
Ammonoids evolutionary rates

ABSTRACT

This paper presents the first quantitative study of the Early Jurassic recovery of ammonoids after the end-Triassic mass extinction based on detailed U–Pb ID-TIMS (isotope dilution thermal ionization mass spectrometry) geochronology from ash bed zircons placed within a clear phylogenetical and biochronological framework at the subzonal and species level. This study was triggered by the discovery of a rich Peruvian succession of ammonites, deposited concomitantly with an unusually large number of ash beds. Two major phases of rediversification are observed during the *Psiloceras spelae* and *Angulaticeras* zones that correspond to positive peaks in the $\delta^{13}C_{org}$ curve, providing a possible link between biodiversity and the global carbon cycle.
In the case of the post-extinction recovery, the development of the earliest Hettangian ammonites occurs within the genus *Psiloceras*, which begins with the occurrence of *P. spelae* and then explodes into worldwide development of smooth psiloceratids of the *Psiloceras planorbis* group s.l. This rapid biodiversification likely occurred less than 100 ka after the end-Triassic crisis; the genus *Psiloceras* occupied all the possible ecological niches worldwide, from the Pacific deep waters to the NW European shallow deposits and also in some rare Tethyan occurrences like at Germig in Tibet. This global dispersion allowed the differentiation of the group in several major phyla, the *Schlotheimiidae, Discamphiceratinae, Arietitidae* and *Lytocerataceae*, which were the roots of all other Jurassic and Cretaceous ammonites.

1. Introduction

Despite the importance of mass extinction events on biological evolution, global climate and geochemical cycling, quantitative models for the rates, causes, and consequences of biotic re-proliferation following these catastrophic events are still lacking. The Triassic–Jurassic boundary (TJB) represents one of the most important biotic crises in Earth history. The end-Triassic mass extinction involved the disappearance of ~80% of all known species on land and in the sea (Jablonski, 1996). Widespread magmatic activity of the Central Atlantic Magmatic Province (CAMP) has been invoked as a cause for this catastrophic biotic event (Courtillot et al., 1999; Marzoli et al., 1999, 2011; Hesselbo et al., 2002), but the relationship between the extinction and its probable volcanic cause can only be established by demonstrating the synchrony of the two events. This requires accurate and precise age determinations for both the TJB strata in a calibrated marine section and of volcanic rocks of the CAMP. New zircon U–Pb ages have been published recently (Schoene et al., 2010a), demonstrating the same age of the earliest Jurassic ammonite *Psiloceras spelae* in both Peru and in Nevada, and these occur within geochronological uncertainty of ca. 150 ka to the onset of the CAMP in North America. The direct comparison among U–Pb dates avoids the discussion about systematic offset between Ar–Ar and U–Pb geochronometers, an important obstacle in obtaining a reliable time frame for cause and effect of extinction events at geological boundaries (Min et al., 2000; Kuiper et al., 2008). The results of Schoene et al. (2010a) are consistent with a model proposed by Guex et al. (2004), who suggested that the main environmental stresses may have been generated by repeated release of SO_2 gas, heavy metal emissions, darkening and subsequent cooling, causing an important eustatic fall. This phase was followed by a major long term CO_2 accumulation during the early Hettangian. However, there is

* Corresponding author.
E-mail address: Jean.Guex@unil.ch (J. Guex).

0031-0182/$ – see front matter © 2012 Elsevier B.V. All rights reserved.
doi:10.1016/j.palaeo.2012.04.030

still substantial uncertainty regarding the fluxes and combined effects of CO_2 and SO_2 into the atmosphere on the plant turnover (Tanner et al., 2007; McElwain et al., 2009), the synchroneity and extent of sea level change recorded in many stratigraphic sections world-wide (Hesselbo et al., 2002; Galli et al., 2007), and disparate chronologies resulting from magneto-, cyclo-, and biostratigraphic calibrations (Cirilli et al., 2009; Ruhl et al., 2010; Whiteside et al., 2010; Marzoli et al., 2011).

Understanding the effects of mass extinctions on the biosphere requires better time-integrated calibrations of recovery patterns following such events. Most of the published compilations of diversity suffer from very low temporal stratigraphic resolution, often at the stage level, as noted by Lucas (1994) and Tanner et al. (2004), and therefore the tempo and mode of extinctions and/or radiations cannot be resolved

This paper presents the first high-resolution quantitative study of the recovery of ammonoids after one of Earth's major extinction events. The main goals of the paper are i) to build a detailed chronostratigraphy across the TJB combining ammonite biostratigraphy, chemostratigraphy and geochronology, and ii) to examine the relationship between ammonite rediversification and the carbon and strontium isotope record.

The discovery of a rich Peruvian succession of ammonites, deposited concomitantly with ash beds containing zircon (Schaltegger et al., 2008; Schoene et al., 2010a), provides a foundation of high-precision U–Pb time constraints within a clear phylogenetical framework and a biochronological analysis at the subzonal level. This paper expands on earlier work with eight new U–Pb ages spanning ca. 4 Ma from the middle Rhaetian to the Hettangian–Sinemurian boundary (HSB), and use this architecture to construct a global synthesis of ammonoid recovery coupled to the carbon isotope record. These geochronological tie-points and biostratigraphic synthesis help calibrate the rates of Rhaetian to Sinemurian ammonite fauna evolution during the critical pre- to post-extinction interval.

2. Regional geology and stratigraphy

The Pucara Formation in the Utcubamba Valley (Northern Peru) hosts one of the best sedimentary records straddling the TJB in the world. The detailed palaeogeography of the Pucara basin in northern Peru is not well established. However, stratigraphic constraints indicate a south to north deepening trend of marine strata near the TJB in the Utcubamba Valley. Much shallower water depths 20 km south of Suta near Chilingote (see Fig. 1) are recorded by carbonate-rich beds with abundant ammonites. Unfortunately, the Chilingote section did not yield any ash beds in the lower Hettangian. The stratigraphic succession near Suta is of intermediate thickness, and the thickest, carbonate poor, unit is located to the north at Levanto where numerous tuff beds have been collected. The original palaeogeographic scheme of Rosas et al. (2007) indicates a Toarcian volcanic arc to the west of the Pucara basin; the existence of ash beds throughout the Upper Triassic (upper Norian) up to the lowermost Sinemurian rather points to a continuous arc-related volcanic activity, which may be located near the present-day coastline. The presence of 900 Ma inherited zircons in some ash beds (Schoene et al., 2010a) indicates that the melts passed through autochthonous upper-middle Proterozoic crust, as has already been identified by Miskovic et al. (2009) and Miskovic and Schaltegger (2009).

The Levanto section is a thick and complete deep marine succession of siltstones alternating with slightly more calcareous silty beds, and is exposed along a new road from Levanto to Maino (Fig. 1). More than

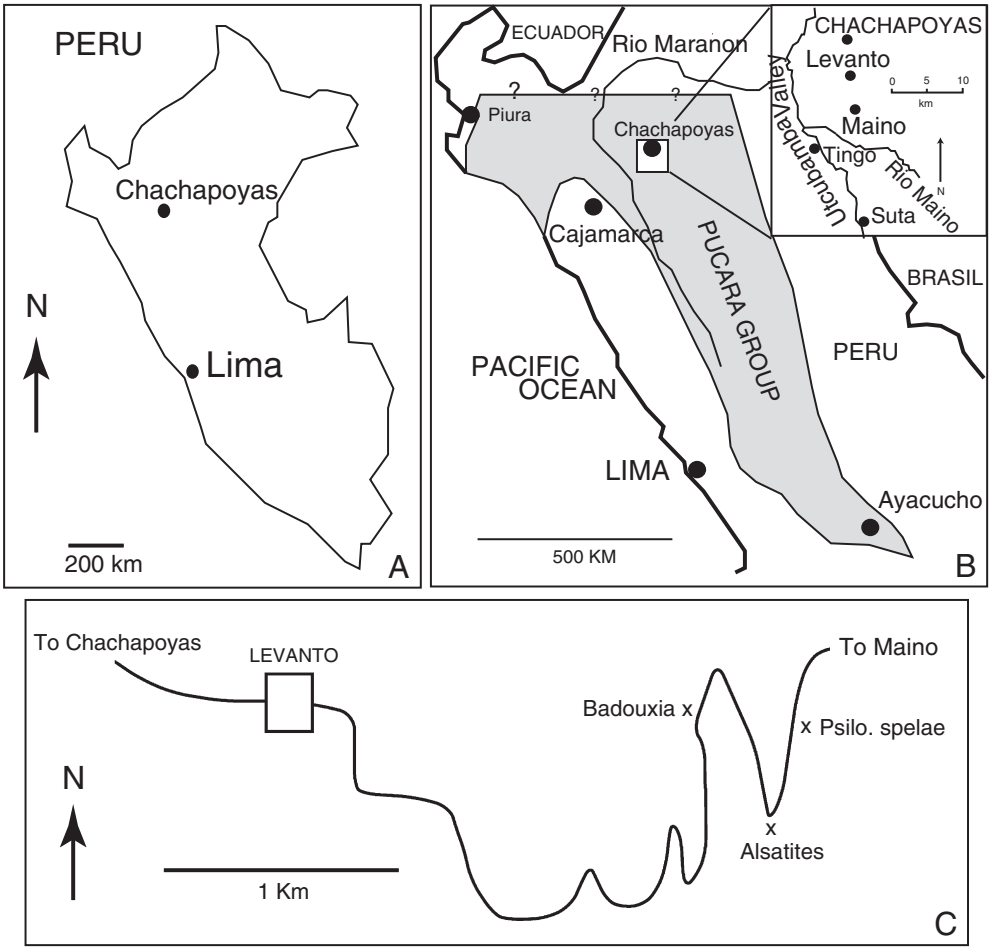

Fig. 1. Location of the studied section and detailed map of the Levanto–Maino road with the location of some marker ammonites.

20 fossiliferous beds have been excavated, allowing a very precise correlation with the standard ammonoid zonations used in the upper Rhaetian - Lower Jurassic (Guex, 1995; Taylor and Guex, 2002; Guex et al., 2004). The TJB is defined by the first occurrence of *P. spelae* (Fig. 2), bracketing a barren interval of some 6 metres for the extinction interval. The Hettangian–Sinemurian boundary is bracketed by *Badouxia canadensis* and *Coroniceras*, leaving an ~15 m thick barren interval for this boundary (Schaltegger et al., 2008). Four major ammonite faunas have been located between these boundaries in the Peruvian succession: *Psiloceras tilmanni, Kammerkarites, Alsatites* and first abundant *Angulaticeras*, allowing a precise calibration of that succession with the units described in Nevada and Oregon (Guex, 1995; Taylor and Guex, 2002).

3. U–Pb isotopic data

Table 1 presents single grain U–Pb zircon data from eight ash beds, obtained by chemical abrasion isotope dilution thermal ionization mass spectrometry (CA-ID-TIMS; see Online Material, Appendix 1). Additional data from three ash beds near the TJB were presented in Schoene et al. (2010a). All data were determined in the same laboratory using the same (^{202}Pb–)^{205}Pb–^{233}U–^{235}U tracer solution, alleviating any systematic biases related to the laboratory or tracer solution used. Uncertainties both in uranium decay constants and tracer calibration (Schoene et al., 2010a) are ignored when calculating the durations of ammonite zones throughout the Hettangian recovery interval. These sources of systematic uncertainty, in addition to that of the composition of natural U (here assumed as ^{238}U/^{235}U = 137.88), should be considered only when comparing these data to U–Pb data generated using a different tracer solution or to another dating technique (such as ^{40}Ar/^{39}Ar).

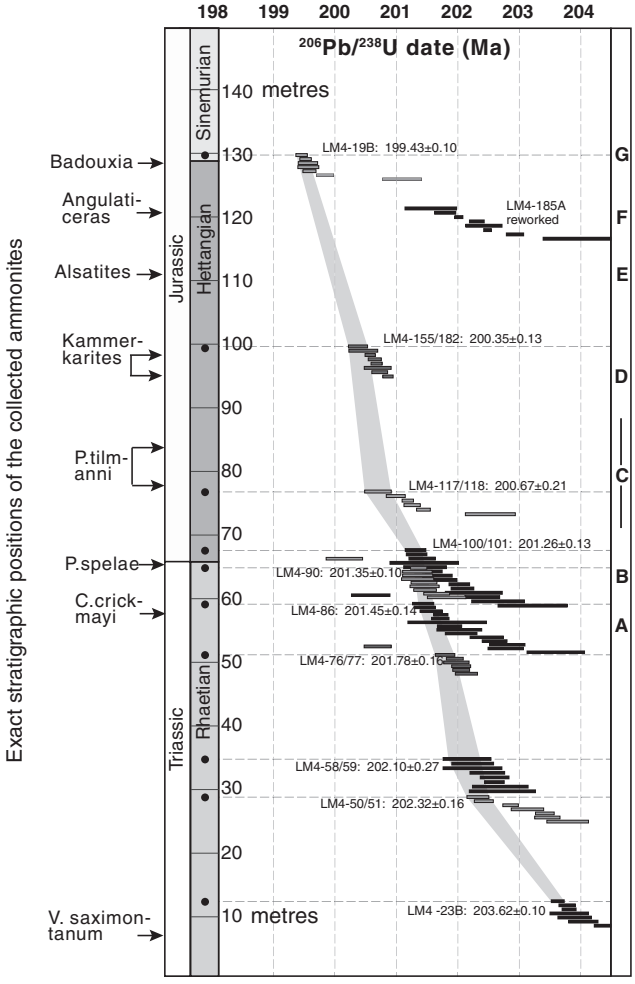

Fig. 2. Stratigraphic column for the Pucara basin section, Peru, with summarized ammonite biostratigraphy, locations of sampled ash beds and resulting U–Pb geochronology. The exact position of each collected ammonite is indicated by an arrow. Ash bed locations are plotted as black dots at the correct stratigraphic height. U–Pb ID-TIMS dates from single zircons is represented by the black and gray bars. The width of the bar is the 95% c.l. uncertainties. Alternating black and grey bars represent analyses from different samples, and the youngest zircon from the main population is interpreted as the eruption age, and this analysis is placed at the correct stratigraphic height at the horizontal dashed lines. The gray band connecting different samples is the result of the age model produced by a Monte Carlo simulation using U–Pb data as inputs, and taking advantage of the constraint of stratigraphic continuity (see text). The resulting recalculated age for ash bed deposition is written next to the sample name. A to G indicate the time diagnostic faunas which are calibrated with the U–Pb ages.

The ^{206}Pb/^{238}U dates for individual zircons from both studies are plotted in Fig. 2 as a function of stratigraphic height. Zircon ^{206}Pb/^{238}U dates from each sample span over between ~0.5 to >2 Ma. A traditional interpretation of similar datasets showing spreads in ^{206}Pb/^{238}U zircon dates beyond analytical scatter is to assume some of the spread is related to Pb-loss and inheritance and the remaining scatter is due to anticipated analytical error (Mundil et al., 2004; Ovtcharova et al., 2006; Ramezani et al., 2007; Davydov et al., 2010). This approach assumes that a subset of the ash bed zircons crystallized over a short period of time relative to the analytical uncertainty immediately before eruption; taking a weighted mean of these data would most accurately and precisely date the eruption. Some of the samples from this study are amenable to this approach—removing several older and younger grains can result in a population that yields a weighted mean with a reasonable MSWD (mean square weighted deviation). Other samples, however, yield no such population and demand a different approach. Given uncertainties of between 100 and 300 ka, those zircon populations clearly represent non-equivalent distributions that can be the result of a) analytical scatter, b) Pb-loss, and c) pre-eruptive growth of zircon.

Analytical scatter, for example underestimation of uncertainties, is not responsible for the observed spread in dates. Careful analysis of the sources and magnitude of U–Pb ID-TIMS uncertainties (Schmitz and Schoene, 2007; McLean et al., 2011) allows identification and quantification of the most important potential sources of systematic or random uncertainties in this study. In particular random uncertainties such as Pb-blank composition have been carefully documented, which is very important in low-Pb zircons. Other important sources include U-oxide isotopic composition (Condon et al., 2010; see analytical details in Online Appendix 1) and Pb and U mass fractionation (here monitored using the ^{202}Pb–^{205}Pb–^{233}U–^{235}U tracer). A test of whether these calibrations are done accurately comes from dating well-behaved zircons generated over the same study period in the same laboratory. Over the course of this study, such zircons have shown remarkable reproducibility better than 0.05% on weighted-mean dates (e.g. the Plesovice zircon from Sláma et al., 2008; the North Mountain Basalt from Schoene et al., 2010a). Those same studies have provided robust intercomparisons with other laboratories dating the exact same samples using the same U–Pb tracer, again giving credence to the accuracy of the dates from this study.

The consistency of dates from some high-U zircon (again, e.g., Plesovice and the North Mountain Basalt) also lends support to the ability of the chemical abrasion technique (Mattinson, 2005) to remove portions of zircon that have lost Pb. Nonetheless, Schoene et al. (2010a) argue that some zircons that are significantly younger than the main population in a sample have been effected by Pb-loss. This apparent discrepancy is probably partly due to the necessity of selecting non-ideal zircons for analysis from ash beds. The ash beds from the present study typically contained <30 zircons, and only a fraction of these had sharp crystal terminations indicative of a magmatic origin. Thus, in all but a couple samples, every zircon in the ash was utilized for chemical abrasion and nearly every zircon was analyzed. Thus, following the interpretation of Schoene et al. (2010a), the efficacy of chemical abrasion is

Table 1
U–Th–Pb isotopic data.

	Compositional parameters				Radiogenic isotope ratios								Isotopic ages					
	Th	Pb*	Pb_c	^{206}Pb	^{208}Pb	^{207}Pb		^{207}Pb		^{206}Pb		corr.	^{207}Pb		^{207}Pb		^{206}Pb	
Sample (a)	U (b)	Pb_c (c)	(pg) (c)	^{204}Pb (d)	^{206}Pb (e)	^{206}Pb (e)	% err (f)	^{235}U (e)	% err (f)	^{238}U (e)	% err (f)	coef.	^{206}Pb (g)	± (f)	^{235}U (g)	± (f)	^{238}U (g)	± (f)
LM4-19B																		
z3	0.739	84	1.78	4798	0.235	0.050169	0.091	0.217450	0.144	0.031436	0.089	0.794	202.82	2.12	199.79	0.26	199.53	0.17
z4	0.633	14	3.08	833	0.201	0.050174	0.445	0.219180	0.508	0.031683	0.168	0.513	203.06	10.34	201.23	0.93	201.07	0.33
z5	0.686	13	1.15	741	0.219	0.050330	0.556	0.218451	0.599	0.031479	0.068	0.673	210.25	12.88	200.62	1.09	199.80	0.13
z6	0.549	37	0.79	2204	0.175	0.050097	0.190	0.217159	0.219	0.031439	0.055	0.617	199.50	4.42	199.54	0.40	199.55	0.11
z7	0.575	86	0.66	5130	0.183	0.050156	0.099	0.217286	0.130	0.031420	0.049	0.751	202.24	2.29	199.65	0.24	199.43	0.10
z9	0.518	126	1.07	7571	0.165	0.050128	0.070	0.217222	0.106	0.031428	0.048	0.847	200.94	1.63	199.60	0.19	199.48	0.09
z11	0.714	17	0.88	1016	0.228	0.050322	0.420	0.218098	0.459	0.031434	0.080	0.551	209.87	9.74	200.33	0.83	199.52	0.16
LM4-185A																		
z1	0.560	8.3	3.84	509	0.178	0.050101	0.747	0.220907	0.796	0.031979	0.072	0.699	199.66	17.35	202.66	1.46	202.92	0.14
z2	0.477	23	0.59	1441	0.152	0.050274	0.257	0.221165	0.274	0.031906	0.032	0.594	207.68	5.95	202.88	0.50	202.47	0.06
z3	0.545	18	1.68	1100	0.173	0.050098	0.353	0.220201	0.379	0.031878	0.061	0.497	199.55	8.20	202.08	0.69	202.29	0.12
z4	0.630	1.4	1.74	98	0.205	0.051603	4.610	0.228860	4.904	0.032166	0.353	0.845	267.85	105.7	209.26	9.27	204.09	0.71
z5	0.486	49	0.81	2992	0.155	0.050152	0.127	0.220115	0.138	0.031832	0.033	0.457	202.05	2.94	202.01	0.25	202.00	0.07
z9	0.633	3.8	0.85	241	0.203	0.050485	1.768	0.222037	1.882	0.031898	0.146	0.792	217.37	40.93	203.60	3.47	202.42	0.29
z10	0.571	17	0.90	1035	0.182	0.050370	0.412	0.220819	0.444	0.031795	0.081	0.478	212.11	9.54	202.59	0.82	201.77	0.16
z11	0.581	7.6	0.83	469	0.186	0.050510	0.962	0.221178	1.042	0.031759	0.212	0.466	218.53	22.25	202.89	1.92	201.55	0.42
LM4-155-182																		
z2	0.774	14	1.71	787	0.246	0.050179	0.484	0.218732	0.515	0.031615	0.047	0.696	203.28	11.22	200.85	0.94	200.65	0.09
z3	0.798	7.8	1.18	451	0.255	0.050412	0.963	0.219518	1.028	0.031581	0.123	0.576	214.04	22.29	201.51	1.88	200.44	0.24
z5	0.815	44	0.53	2485	0.259	0.050125	0.164	0.218379	0.178	0.031598	0.039	0.460	200.81	3.80	200.56	0.32	200.54	0.08
z6	0.707	22	0.45	1248	0.225	0.050248	0.334	0.218707	0.360	0.031568	0.066	0.476	206.47	7.73	200.83	0.66	200.35	0.13
z7	0.870	25	0.72	1366	0.277	0.050229	0.301	0.219146	0.323	0.031643	0.044	0.535	205.59	6.99	201.20	0.59	200.82	0.09
z8	0.884	15	0.86	856	0.282	0.050225	0.515	0.219002	0.550	0.031625	0.069	0.561	205.42	11.94	201.08	1.00	200.71	0.14
z9	0.834	16	0.81	927	0.265	0.050164	0.434	0.218644	0.464	0.031611	0.056	0.574	202.62	10.08	200.78	0.85	200.62	0.11
z10	0.851	7.1	0.87	411	0.273	0.050606	1.034	0.220618	1.103	0.031618	0.109	0.661	222.94	23.92	202.42	2.02	200.67	0.21
LM4-117-118																		
z1	0.582	8.0	0.65	493	0.186	0.050506	0.859	0.220514	0.914	0.031666	0.079	0.726	218.34	19.87	202.34	1.68	200.97	0.16
z2	0.631	14	0.63	848	0.201	0.050341	0.481	0.220093	0.515	0.031709	0.064	0.567	210.78	11.16	201.99	0.94	201.23	0.13
z3	0.482	32	0.87	1962	0.153	0.050148	0.260	0.219165	0.279	0.031697	0.045	0.495	201.87	6.02	201.21	0.51	201.16	0.09
z5	0.514	2.0	3.97	138	0.165	0.050680	3.001	0.223003	3.192	0.031913	0.206	0.934	226.33	69.35	204.41	5.91	202.51	0.41
z6	0.434	1.7	10.72	125	0.141	0.051424	1.564	0.235273	1.668	0.033182	0.320	0.409	259.89	35.93	214.54	3.23	210.43	0.66
z8	0.391	23	1.47	1431	0.125	0.050230	0.270	0.219807	0.291	0.031738	0.054	0.474	205.65	6.26	201.75	0.53	201.42	0.11
z10	0.851	7.1	0.87	411	0.273	0.050606	1.034	0.220618	1.103	0.031618	0.109	0.661	222.94	23.92	202.42	2.02	200.67	0.21
LM4-76-77																		
z1	0.624	20	0.97	1194	0.199	0.050256	0.350	0.220498	0.384	0.031821	0.068	0.571	206.84	8.11	202.32	0.70	201.94	0.14
z3	0.462	10	0.73	632	0.147	0.050419	0.700	0.221241	0.754	0.031825	0.101	0.591	214.35	16.20	202.94	1.39	201.96	0.20
z5	0.713	14	0.75	803	0.228	0.050368	0.508	0.220826	0.545	0.031798	0.083	0.506	211.99	11.76	202.60	1.00	201.79	0.17
z6	0.736	11	0.80	629	0.235	0.050474	0.650	0.221560	0.694	0.031837	0.082	0.582	216.86	15.04	203.21	1.28	202.03	0.16
z7	0.607	13	0.58	775	0.194	0.050376	0.574	0.221245	0.615	0.031853	0.087	0.526	212.40	13.29	202.95	1.13	202.13	0.17
z8	0.676	20	0.65	1149	0.216	0.050310	0.371	0.220850	0.399	0.031838	0.067	0.490	209.35	8.60	202.62	0.73	202.04	0.13
z10	0.851	7	0.87	411	0.273	0.050606	1.034	0.220618	1.103	0.031618	0.109	0.661	222.94	23.92	202.42	2.02	200.67	0.21
LM4-58-59																		
z2	0.607	3.7	0.55	237	0.190	0.049263	1.948	0.216361	2.072	0.031854	0.195	0.663	160.36	45.56	198.88	3.74	202.14	0.39
z3	0.633	3.5	0.86	221	0.205	0.051115	2.012	0.224593	2.150	0.031867	0.242	0.609	246.03	46.33	205.73	4.00	202.22	0.48
z4	0.641	3.9	0.72	244	0.207	0.051106	1.716	0.224549	1.830	0.031867	0.174	0.682	245.59	39.52	205.69	3.41	202.22	0.35
z5	0.763	5.6	0.42	333	0.245	0.050779	1.351	0.223634	1.453	0.031942	0.233	0.500	230.79	31.20	204.93	2.70	202.69	0.46
z6	0.654	9.1	0.63	545	0.208	0.050132	0.748	0.220679	0.797	0.031926	0.077	0.661	201.13	17.36	202.47	1.46	202.59	0.15
z7	0.650	3.8	1.14	237	0.207	0.050307	1.719	0.221321	1.829	0.031907	0.147	0.771	209.22	39.84	203.01	3.37	202.47	0.29
z8	0.501	4.0	0.74	257	0.160	0.050405	1.555	0.221874	1.654	0.031925	0.113	0.885	213.73	36.01	203.47	3.05	202.58	0.22
z9	0.724	5.6	0.60	338	0.229	0.049910	1.244	0.219815	1.349	0.031942	0.282	0.462	190.81	28.94	201.76	2.47	202.69	0.56
z10	0.508	0.8	1.06	68	0.168	0.052578	7.740	0.235136	8.224	0.032435	0.583	0.841	310.63	176.2	214.43	15.90	205.77	1.18
LM4-50-51																		
z1	0.889	8.4	0.87	476	0.284	0.050542	0.861	0.223449	0.924	0.032064	0.104	0.645	220.01	19.92	204.78	1.71	203.46	0.21
z3	0.845	16	0.82	919	0.270	0.050441	0.445	0.222957	0.484	0.032058	0.072	0.594	215.36	10.30	204.37	0.90	203.42	0.14
z4	0.822	10	1.19	563	0.263	0.050437	0.714	0.221704	0.768	0.031881	0.086	0.658	215.17	16.54	203.33	1.42	202.31	0.17
z8	0.964	4.3	1.43	247	0.310	0.050831	1.722	0.225096	1.835	0.032117	0.171	0.690	233.15	39.73	206.14	3.42	203.79	0.34
z9	0.946	5.1	1.00	291	0.303	0.050671	1.496	0.223656	1.593	0.032012	0.132	0.753	225.91	34.58	204.95	2.96	203.13	0.26
z10	0.790	10	0.78	597	0.250	0.049994	0.673	0.219871	0.717	0.031897	0.078	0.615	194.71	15.63	201.80	1.31	202.41	0.15
z11	0.928	9.4	1.18	527	0.296	0.050231	0.730	0.221401	0.777	0.031967	0.061	0.785	205.72	16.94	203.08	1.43	202.85	0.12
LM4-23B																		
z1	0.972	22	0.76	1198	0.310	0.050350	0.337	0.222781	0.361	0.032091	0.052	0.520	211.17	7.81	204.22	0.67	203.62	0.10
z2	0.822	15	0.70	844	0.262	0.050308	0.484	0.222803	0.516	0.032121	0.056	0.618	209.23	11.21	204.24	0.96	203.81	0.11
z3	0.759	10	0.94	585	0.242	0.050324	0.657	0.222851	0.700	0.032117	0.066	0.681	209.98	15.22	204.28	1.29	203.79	0.13

Table 1 (*continued*)

	Compositional parameters				Radiogenic isotope ratios								Isotopic ages					
	Th	Pb*	Pb_c	^{206}Pb	^{208}Pb	^{207}Pb		^{207}Pb		^{206}Pb		corr.	^{207}Pb		^{207}Pb		^{206}Pb	
Sample (a)	U (b)	Pb_c (c)	(pg) (c)	^{204}Pb (d)	^{206}Pb (e)	^{206}Pb (e)	% err (f)	^{235}U (e)	% err (f)	^{238}U (e)	% err (f)	coef.	^{206}Pb (g)	± (f)	^{235}U (g)	± (f)	^{238}U (g)	± (f)
LM4-23B																		
z4	0.759	5.7	1.54	339	0.242	0.050430	1.190	0.223447	1.270	0.032136	0.134	0.629	214.85	27.56	204.77	2.35	203.90	0.27
z5	0.806	5.0	1.40	296	0.258	0.050575	1.340	0.224255	1.427	0.032160	0.114	0.778	221.49	30.99	205.45	2.65	204.05	0.23
z6	0.839	8.8	0.92	503	0.270	0.050791	1.040	0.225685	1.110	0.032227	0.126	0.598	231.35	24.00	206.63	2.07	204.47	0.25
z7	0.846	3.5	1.27	214	0.270	0.050517	1.877	0.223731	1.997	0.032121	0.156	0.790	218.84	43.42	205.01	3.71	203.81	0.31

(a) z1, z2, etc. are labels for fractions composed of single zircon grains or fragments; all fractions annealed and chemically abraded after Mattinson (2005).
(b) Model Th/U ratio calculated from radiogenic 208Pb/206Pb ratio and 207Pb/235U age.
(c) Pb* and Pbc represent radiogenic and common Pb, respectively.
(d) Measured ratio corrected for spike and fractionation only. Mass fractionation correction of 0.13 ± 0.02 (1-sigma) %/amu (atomic mass unit) was applied to ET535-spiked samples based on values determined from ET2535-spiked samples.
(e) Corrected for fractionation, spike, and common Pb; all common Pb was assumed to be procedural blank:
206Pb/204Pb = 18.39 ± 0.60%; 207Pb/204Pb = 15.62 ± 0.66%; 208Pb/204Pb = 37.62 ± 0.78% (uncertainties 1-sigma standard deviations of blank determinations).
206Pb/238U and 207Pb/206Pb ratios corrected for initial disequilibrium in 230Th/238U using Th/U [magma] = 4.
(f) Errors are 2-sigma, propagated using the algorithms of Schmitz and Schoene (2007) and Crowley et al. (2007).
(g) Calculations are based on the decay constants of Jaffey et al. (1971).

assumed and the youngest zircon from the main population is used as the best estimate of eruption age, interpreting older grains as the result of zircon growth prior to ash bed deposition. One sample from this study (LM4-76/77) has a younger grain that is attributed to Pb-loss (two grains from LM4-90 and LM4-86, plotted in Fig. 2, were interpreted similarly in Schoene et al., 2010a). One other sample (LM4-50/51) has two grains that are younger and do not overlap within error with older zircons. In this case, the younger grains are interpreted as magmatic, though using the youngest grain from the older population will have little effect on our interpretations because this sample does not fall near an important biostratigraphic marker.

It is also important that the arguments for Pb-loss and pre-eruptive growth of zircon given below and in Schoene et al. (2010a) are supported by the fact that using this interpretation produces the expected age progression (younging upwards) in the stratigraphic succession. One notable exception is that of sample LM4-185A, whose zircons fall much older than several lower ash beds. That sample is interpreted as representing reworked volcanic material, transported as submarine gravity flows originating from older sediment.

With the exception of sample LM4-185A, the spread in zircon dates is interpreted to be primarily the result of pre-eruptive growth of zircon, the youngest of these populations as the best estimate for the time of ash bed deposition. Possible sources for zircon predating the eruption include xenocrystic zircon from the host rock to the magmatic system (i.e. the country rock), antecrystic zircon from slightly older portions of the magmatic system, zircon entrained in the ash and debris plume during eruption, or zircon grown in a magma chamber leading up to eruption (e.g. Bacon and Lowenstern, 2005; Charlier et al., 2005; Simon and Reid, 2005; Bachmann et al., 2007; Crowley et al., 2007; Miller et al., 2007; Schaltegger et al., 2009; Wilson and Charlier, 2009; Bachmann et al., 2010; Schmitt et al., 2010, 2011). Both U–Pb and U-series methods in the above-cited studies have documented that zircon populations have dates anywhere from 0 to >500 ka older than the eruption. Simon et al. (2008), using a smaller dataset than is now available, estimate that the "average" age offset in zircon due to pre-eruptive growth was ~80 ka. Though the datasets from each ash bed in this study are lower-N than is normal for *in situ* methods, if the age distributions are in fact affected by pre-eruptive zircon growth, zircons both older and younger than the average offset were likely sampled. Given the uncertainties on individual grains of >100 ka, it is very likely that the youngest grain overlaps with the true eruption age if the sampled layers are primary ash beds.

The exact origin of pre-eruptive zircons is not obvious, though zircon geochemical data analyzed in concert with U–Pb geochronology (U–Pb TIMS-TEA; Schoene et al., 2010b) from one of the ash beds presented in Schoene et al. (2010a) show remarkable heterogeneity. Schoene et al. (2010b) argue that the lack of coherent geochemistry from zircons from a single ash bed support an inherited origin for those grains—either as antecrysts or entrained material during eruption. Regardless of their exact origin, the observation that even a subset of zircon from an ash bed may not be cogenetic demands caution when taking weighted-means of zircon populations. Several samples, on the other hand, show trends in time with Th/U, consistent with growth of zircon in an evolving magmatic system (e.g. LM4-155/182, LM4-117/118, LM4-58/59, and LM4-50/51). This observation supports an antecrystic origin for zircon from these samples.

Several samples (e.g. LM4-90, LM4-19B) yield zircon populations amenable to weighted mean $^{206}Pb/^{238}U$ dates with reasonable MSWDs. In such a case, a weighted mean may be the most precise estimate of eruption without sacrificing accuracy. However, the youngest grain is still considered as the best estimate of eruption date. This is a more conservative approach in light of recent datasets documenting pre-eruptive zircon growth that may be small relative to the analytical scatter. Using his interpretation, the youngest grain of such a dataset will still overlap the weighted mean. This approach sacrifices the increased precision afforded by weighted-means, but does not risk inaccuracy.

The U–Pb data can be used to build an age model for the deposition of the Rhaetian–Sinemurian section from the Pucara basin in Peru. Average deposition rates between ash beds range from 13 to 68 mm/ka, with an average of 36 ± 18 mm/ka (± 1 standard deviation). Because of such low sedimentation rates and an abundance of ash beds, estimated deposition ages from many ash beds overlap with those above and below them. The result is that events bracketed by these ash beds cannot be determined with high precision. However, the additional constraint that an ash bed higher in the sequence must be younger than the one beneath it can be built into the age model using a simple Monte Carlo simulation. This model produces 10^6 normally distributed numbers for each ash bed that correspond to the age and uncertainty of the youngest zircon from an ash bed. It then randomly pulls a value from each ash bed distribution to produce a model for age versus height, resulting in 10^6 age models. If any ash bed is older than the one beneath it, that age model is discarded. The remaining age models (~400,000) are used to generate a new deposition age for each ash bed. In most cases, the resulting deposition age is identical to the input, though improved precision is seen in areas of dense ash bed sampling (e.g. near the TJB) or for example with the relatively imprecise data from low-U zircons of sample LM4-58/89. The resulting age versus height model and recalculated deposition ages for ash beds are plotted in Fig. 2 with a grey band. The accuracy of the model depends on how well the dated ash beds represent deposition, and as such it should be noted that many of the sampled ash beds contained a large amount of ash-rich material (now clay) while others were predominantly fine-grained silt. The latter beds may represent

reworked volcanic material, which is the origin of LM4-185A. Assessing the time gap represented between deposition and reworking is impossible, though the striking stratigraphic continuity followed by the dates deserves reiteration: if any of the beds that fall in sequence were reworked material, the time lag was not large. Further work in this section and others that are well calibrated geochronologically and biostratigraphically can be used to address this issue directly.

4. Ammonite biochronology

The age model determined in the previous section can be used to calibrate the timing of classical ammonite zones. For practical reasons, a simplified non-standard zonation is used in the present work, which results from the biochronological syntheses presented below (Fig. 3) and allows for a clear representation of the large-scale correlations.

Ammonite biostratigraphic data from the Pacific Realm (western South and North America), including some data from Kuhjoch in the Austrian Alps (Online Appendix 2), have been critically synthetized and analyzed using the Unitary Association theory (Guex, 1991) and the UA-graph computer program (Hammer et al., 2011). That method is based on graph theory and is designed for the construction of concurrent range zones using a fully deterministic approach. The motivation is to construct a discrete sequence of coexistence intervals of species. Each interval, corresponding to one UA, is of minimal duration while consisting of a maximal set of intersecting ranges. Each UA is characterized by a set of species allowing its identification in the stratigraphic sections. The chronological significance of the units generated by the UA software (http://folk.uio.no/ohammer/uagraph) depends on two important parameters: (i) their lateral traceability (here called 'reproducibility'); and (ii) the superpositional control between two adjacent units. The major difficulties related to the construction of such units are related to the conflicting inter-taxa relationships (= cycles in the biostratigraphical graph G*) and the inter-maximal cliques contradictions (strongly connected components in the maximal clique graph Gk). Such contradictions are generally eliminated by adding virtual coexistences (= edges) in the G* graph. The goal of the method is not to reduce the number of virtual coexistences at all cost, but to produce a robust solution that reflects the quality of the data, i.e. a solution optimizing the reproducibility and inter-unit superpositional control. UAs should be considered as intervals of uncertainty on which an order relation can be established: the UA sequences represent units, which are ordered as older, subcontemporaneous, or younger. The order of the event within a single particular unit is not known (details in Guex and Davaud, 1984; Guex, 1991; see also Mailliot et al., 2006 for an application) because the virtual coexistences between some taxa represent inter-taxa exclusions, which cannot be solved by means of statistical techniques; they can only be solved by the construction of composite stratigraphic sections, whenever possible.

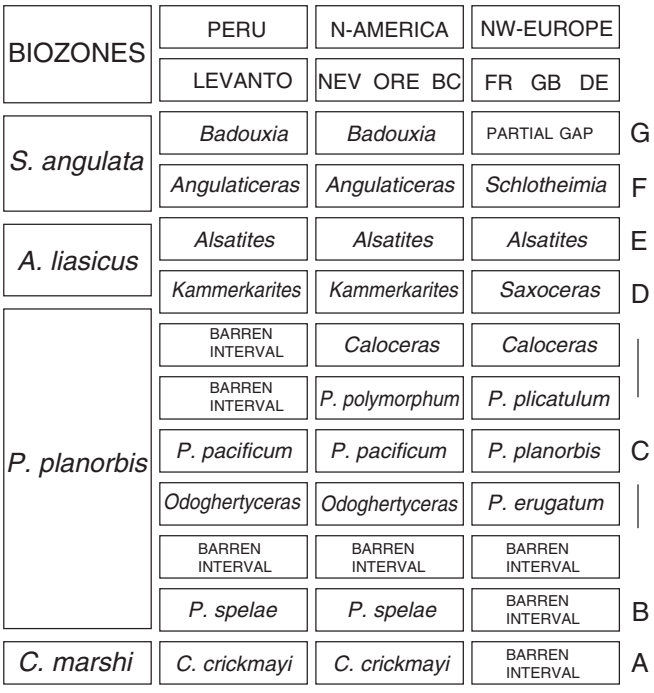

Fig. 3. Informal zonation of the topmost Triassic and lowermost Jurassic. The boxes indicate that the biostratigraphic units used in the present paper are discrete (see Guex, 1991 for details). A to G indicate the faunas which are calibrated in Fig. 2. D' is extrapolated.

The original data used in the present synthesis included the distribution of more than 90 taxa, species and genera from the Pacific realm where dubious data were excluded. The original sources are given in Online Appendix 2. The range chart resulting from that revision is given in Fig. 4, showing the details of the diversification of the ammonites during that interval of time, following the Late Triassic major extinction. For comparison, the same procedure has been applied to the precise biostratigraphic data from sections in England, France and Germany (references in Online Material Appendix 2) to produce a global biochronological framework of the Hettangian ammonite distribution in the NW-European realm. The resulting range chart is given in Fig. 5 and the calibration with the new numerical ages is established using the intercontinental correlation table of Fig. 3. Note that the European record, although studied for more than a century, is less complete than the record established in the Pacific realm.

The range chart in Fig. 5 can be used to calibrate the main units based on the geochronology and ammonite biostratigraphy in the Pacific realm (Figs. 2 and 4). Note also that units A, B and G, are missing. The reason is clear for the lower part of the synthetic section: the upper Rhaetian ammonites and the *P. spelae* zone are missing in the NW European realm. In the upper part of the section, unit G, representing the *Badouxia* fauna, is only partially represented, if at all. Studying the European Hettangian data leads to the obvious conclusion that there is, everywhere in that region, a very important gap straddling the HSB (Hettangian–Sinemurian Boundary), making it unsuitable for a type section for the boundary. In particular, the accepted stratotype for the HSB (Bloos and Page, 2002) at Quantoxhead (Somerset) certainly contains gaps: the boundary beds of the topmost Hettangian contain a very diversified fauna of schlotheimiids, and these beds are abruptly overlain by deposits full of vermiceratids, without a single transitional fauna. This is a typical sign of hiatus due to non-deposition.

5. Variations of the taxonomic richness

The variations of the ammonite species richness (Sobs) is expressed as the total taxonomic richness observed in the interval corresponding to the geochronometrical tie point. These variations (Sobs) throughout the Hettangian for the Pacific and NW European records were constructed respectively from the UA-range charts of Figs. 4 and 5, respectively, and calibrated to the new geochronological data (Fig. 2). The mode and tempo of ammonite recovery (Fig. 6) are derived mainly from the Pacific record, which is more complete than the NW European record. The FO of *P. spelae* (unit B), well recorded in the Pacific and Austrian sections (Fig. 6) marks the base of the Hettangian stage (and of the Jurassic System) and the onset of recovery <290 ka after the end-Triassic mass extinction (unit A). Following this initial recovery a rapid radiation occurs, with a peak of originations both in the Pacific and NW Europe (unit C) (Figs. 6 and 7). Interestingly this rapid and wide peak of originations coincides also with a peak of extinctions: the last Choristoceratacea (i.e., *Choristoceras minutum* and *Odoghertyceras*) surviving the mass extinction were finally extinguished at that time (Fig. 6). But in this case the originations exceeded the extinctions, resulting in an increased diversification trend. Then, both curves from Pacific and NW Europe show a strong slowdown in the diversification of the ammonites (from C to D') during a time

Fig. 4. Pacific Range Chart (N and S America). The Unitary Associations represented on the *x*-axis correspond to the maximal intersections of the ammonite ranges calculated by means of the UA-graph program (Hammer et al., 2011) (see text for details). References in Online material, Appendix 2A.

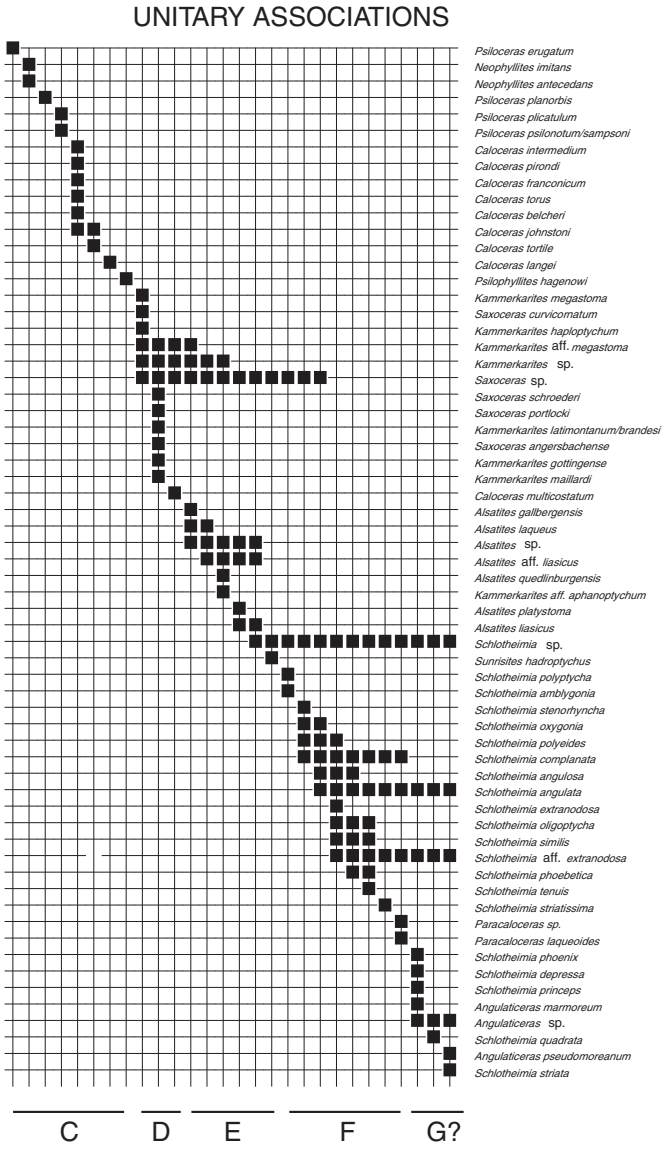

Fig. 5. Range Chart NW Europe: Unitary Associations calculated by means of the UA-graph program (Hammer et al., 2011). A to G correspond to the codes used in Fig. 2. References in Online material Appendix 2B.

interval of about 500 ka, although a decrease in extinctions occurred. Such a slowdown was driven therefore by a dramatic reduction in originations. That interval was followed by a new major pulse (lasting about 1 Ma) of diversification in the upper Hettangian *Alsatites liasicus* and *Schlotheimia angulata* zones (from D' to G). In the NE Europe sections this pulse of diversification was in part driven by the explosion of the schlotheimiids, which is certainly artificially emphasized by a taxonomic oversplitting of this group by the pioneering palaeontologists who first investigated that region (references in Online Material, Appendix 2).

The cumulated FAD–LAD curve of Fig. 8 (see Guex, 1991 for details), derived from the UA-range chart of Fig. 4, shows that the general diversity variation is graphically organized along a straight line, which implies that the originations are roughly compensated by the extinctions, a fact that also appears in the curves given in Fig. 6. A partial correlation between the ammonite diversity fluctuations and the $\delta^{13}C$ of organic matter ($\delta^{13}C_{org}$) is observed in Fig. 6. The simplified $\delta^{13}C_{org}$ curve derives from the Rhetian–Hettangian New York Canyon (Nevada) record directly calibrated with high resolution ammonite biostratigraphy (Bartolini et al., 2012). The well-known end-Triassic negative excursion of the organic carbon is correlated with a peak in ammonite extinctions and an interval of no originations, coinciding with the mass extinction interval (Ward et al., 2001; Guex et al., 2004; Clémence et al., 2010). The second negative excursion is restricted to the *Psiloceras pacificum* zone (equivalent to the *P. planorbis* zone in NW Europe) and coincides with a second pulse of extinctions (unit C), associated with an acceleration of originations.

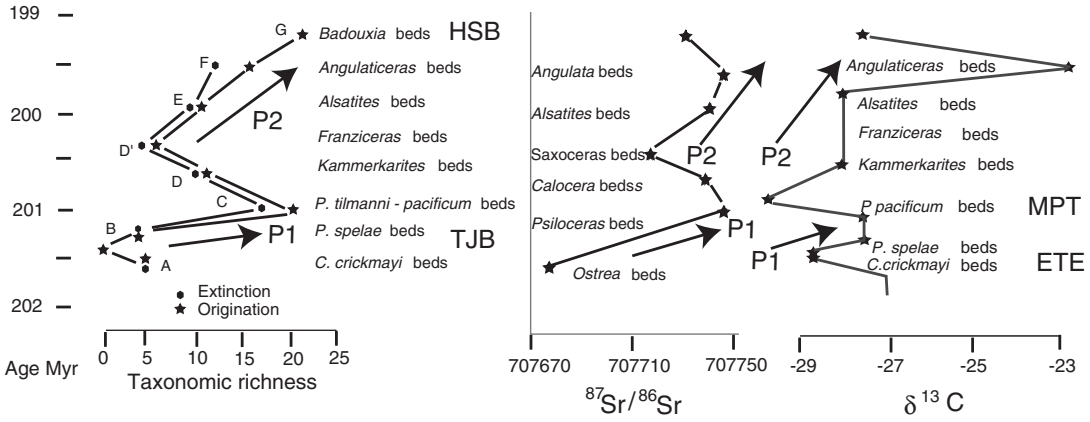

Fig. 6. Variations of the ammonite taxonomic richness (S_{obs}) throughout the Pacific realm Hettangian, calibrated to the new geochronological data. P1 and P2 are the two successive major pulses of diversification. A to G correspond to the codes used in Fig. 2. The precise stratigraphic beds from which the biozone marker ammonites were collected are indicated in the $^{87}Sr/^{86}Sr$ (see text) and the $\delta^{13}C_{org}$ curves. ETE = End Triassic Extinction and MPT = Main Plant Turnover.

This second ammonite crisis coincides also with a major turnover of plants in the continents and a huge increase of pCO_2 in the atmosphere (McElwain et al., 2009; Bartolini et al., 2012). The initial recovery of ammonites is therefore highly stressed, probably by new pulses of CAMP activity and volcanogenic build up of CO_2 in the atmosphere (Bartolini et al., 2012). The mid-Hettangian slow-down of diversification is followed by an explosion of the diversity in the Upper Hettangian correlated with a major positive excursion in $\delta^{13}C_{org}$ values of organic matter (Bartolini et al., 2012). $\delta^{13}C_{org}$ and ammonite diversity curves across the Triassic–Jurassic boundary therefore show multiple crises. The strontium data, based on the measurements of Jones et al. (1994) in Great Britain (see also Cohen and Coe, 2007) are plotted as the mean-values of the original measurements per subzone. There is an apparent correlation between the taxonomic richness and the variation of the $^{87}Sr/^{86}Sr$ ratio. Such a correlation was already observed and discussed by Cardenas and Harries (2010) at a very large scale in the marine Phanerozoic genera. According to these authors, this correlation is controlled by the availability of marine nutrients.

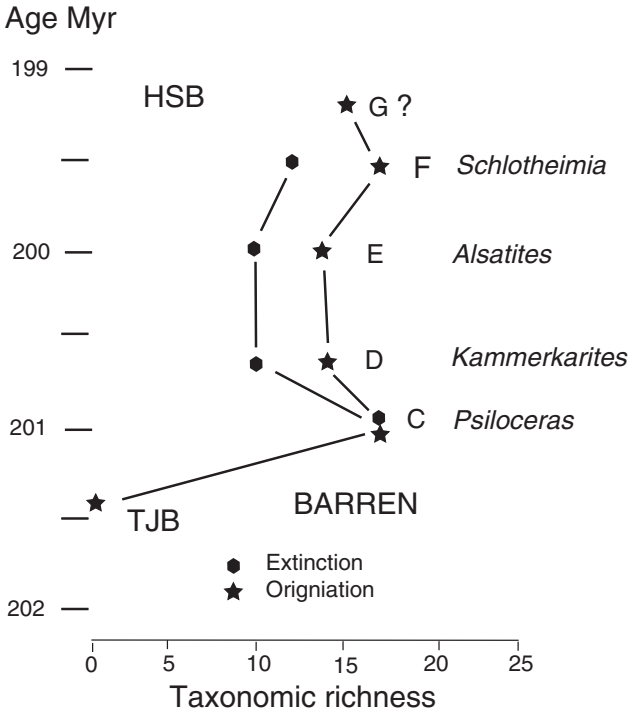

Fig. 7. Rate of diversification of the Hettangian ammonites in NW-Europe. A to G correspond to the codes used in Fig. 2.

6. Rate of changes in ammonoids evolutionary trends

6.1. Increasing involution

The most frequent evolutionary trend observed in Mesozoic ammonites is where the ancestral group has an open umbilicus (i.e. evolute form) and where the descendants are involute (i.e. tightly coiled, oxycone or sphaerocone). This trend was first described in Lower Jurassic ammonites (Hyatt, 1889) and later recognized in Devonian ammonites, at the beginning of the history of the group (Erben, 1966).

The trend towards increasing involution of originally evolute shells leads either to lenticular (oxycones) or more or less spherical shells (sphaerocones). The recurrent character of this trend was discussed in the early 1940s to explain the multitude of heterochronous homeomorphies observed within this group (Schindewolf, 1940; Haas, 1942). Some ammonite lineages also show a broad trend towards increased sinuosity of the growth-lines and, on a large time scale, this group shows an overall increase in suture line complexity.

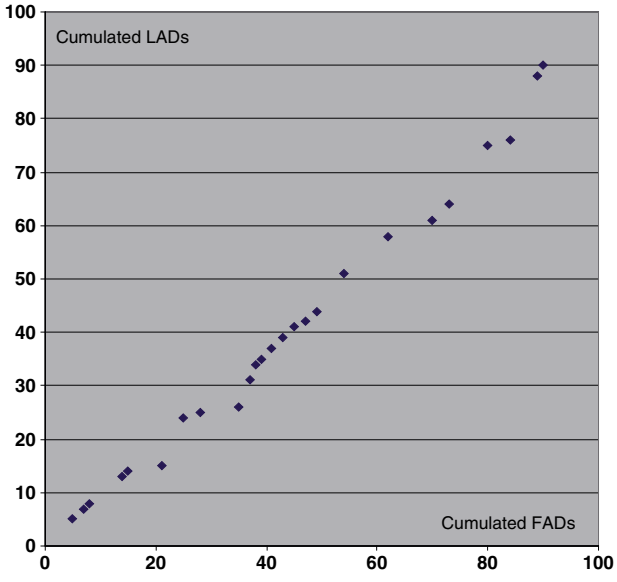

Fig. 8. Cumulated Fads–Lads generated from Fig. 4. The *ij* coordinates express the number *i* of cumulated fads and the number *j* of cumulated lads. When the origination vs extinction rates are constant, the *ij* values are distributed along the diagonal.

Such trends are well represented in most lineages of Fig. 9. They all derived from smooth *Psiloceras* of the Lower Hettangian: *Kammerkaroceras* via *Discamphiceras* (*Discamphiceratinae, Psiloceratacеae*), *Angulaticeras* via *Saxoceras* and *Kammerkarites* (*Schlotheimiidae, Psiloceratacеae*), *Pseudaetomoceras* via *Caloceras* and *Alsatites* (*Arietitidae, Arietitaceae*), *Badouxia* via *Caloceras* and *Sunrisites*.

It is quite obvious that allometries characterizing the geometrical/morphological evolution of shelly invertebrates show that size (i.e. diameter or length), volume and surface vary independently. Within ammonites, an increase in volume, which is not accompanied by an increase in size (i.e. the diameter) will result in an increase of involution. Similarly, a decrease in size which is not accompanied by a decrease in volume will also lead to a drastic increase of involution. Such a process certainly accounts for the geometry of the Early Triassic small cryptogenic sphaerocone ammonites, for example the isculitids deriving from *Columbites*. Note also that an increase in the mantle's surface area, if not compensated by a simultaneous increase in volume of the animal, results in an increase in suture complexity and/or flexuosity of growth lines at the aperture (see Guex, 2003 for details). Thanks to the new geochronological data produced here, the rate of change in the involution can be quantified and expressed by the variation of the ratio U/D (=umbilicus vs diameter) in some typical phylogenetical lineages mentioned above (Fig. 10).

6.2. Proterogenesis

Another major mode of geometrical transformation in ammonoids is when new structures appear at a very early stage of the ancestral development. That kind of transformation, occurring within very short interval of times, is called proterogenesis. It was first discovered by Pavlov (1901) and independently by Spath (1924) and Schindewolf (1925). Three major Hettangian lineages are affected by proterogenesis. The first is the *Schlotheimiidae* where the ventral groove first appears in *Saxoceras*, a group directly related to *Kammerkarites*. Then the groove invades all the ontogeny, giving rise to *Schlotheimia* during the late Hettangian (about 0.5 Myr). The lytoceratids follow the same kind of process. The early stage of some smooth *Psiloceras* of the *Transipsiloceras* group develop the typical very evolute geometry with rounded whorl section and very high rate of whorl expansion, giving rise to *Pleuroacanthites*. The same occurs in the derivative of *Pleuroacanthites, Eolytoceras*, which is the first typical lytoceratid, and *Analytoceras* with a constricted juvenile stage. This occurs within an interval of time of about 1 Myr. A similar transformation is observed in some *Psiloceras* where the ribbing first develop in the ancestral juvenile (e.g. *P. primacostatum*), invading the complete ontogeny in *Caloceras*.

6.3. Stress and uncoiling

The relation between stress and uncoiling in ammonites is widely observed and it has been shown that such evolutionary simplifications of the geometry of ammonites were generally correlated with $\delta^{13}C_{org}$ negative anomalies in the stratigraphical record (Guex, 2003, 2006; O'Dogherty et al., 2006). In the present case, two major abnormal developments of serpenticone ammonites during the Hettangian are observed. The first is characterized by the appearance of serpenticone caloceratids such as *C. multicostatum* in the *P. planorbis* zone which occurs in the early part of the second negative carbon excursion of Guex et al. (2004). The second occurrence of serpenticone ammonites occurs in the *Badouxia* zone (see Taylor and Guex, 2002) with the appearance of serpenticone vermiceratids such as *V. morganense* and *Paradiscamphiceras*. These vermiceratids are perfectly homoeomorphic with the most evolute representative of alsatitids of the middle Hettangian. These two cases of relative uncoiling are concomitant with important sedimentary gaps in the *Caloceras* beds in Nevada and in the interval spanning the HSB in NW Europe.

7. Conclusion

A detailed geochronological framework and a new biochronological analysis at the subzonal level and species level allows us to present the first quantitative study of the recovery of ammonoids after a major extinction (end Triassic). This was made possible by the discovery of a rich Peruvian succession of ammonites, deposited concomitantly with densely spaced, zircon-bearing ash beds amenable to high-precision ID-TIMS U–Pb geochronology. Across the Triassic–Jurassic, the diversification pattern of ammonites is marked by two extinctions events, and two pulses of originations separated by a slowdown of diversification. The two major phases of ammonite rediversification are synchronous with the *P. spelae* and *Angulaticeras* positive peaks of the curve, and the two peaks of extinctions are correlated with the negative excursions in the *C. crickmayi* and *P. planorbis* zones. In the case of the TJ recovery the development of the earliest Hettangian ammonites occurs within the genus *Psiloceras*, which starts with the occurrence of *P. spelae* followed by the worldwide development of smooth psiloceratids of the *P. planorbis* group s.l. That genus literally exploded about 400 to 500 ky after the first occurrence of *P. spelae* and occupied all the possible

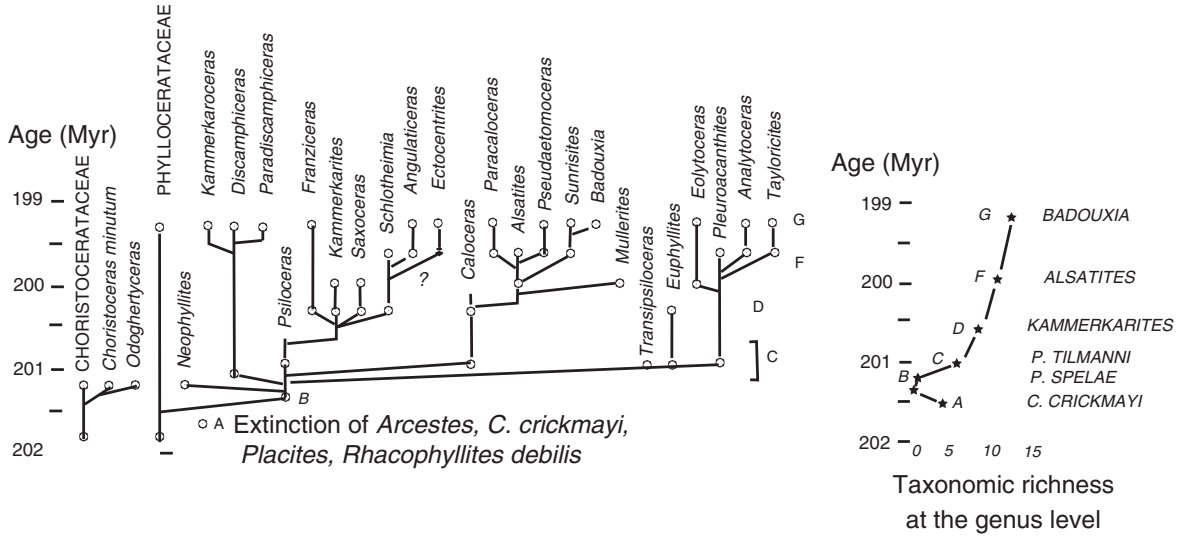

Fig. 9. General phylogenetic framework of the Pacific realm, including some tethyan genera not present in America such as *Tayloricites* (modified from Guex, 1995; Guex et al., 2004). The variations of the generic diversity through the Hettangian are calibrated with the numerical time scale.

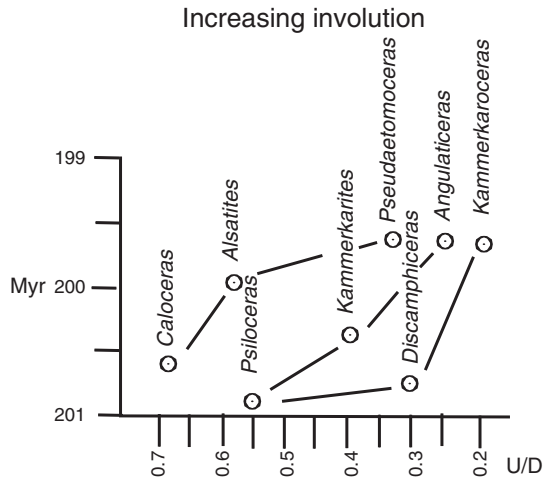

Fig. 10. Rate of increasing involution in the *Discamphiceratinae, Schlotheimiidae* and *Alsatitinae*.

ecological niches all over the world, from the Pacific deep waters to the NW European shallow deposits and also in some Tethyan occurrences like at Germig in Tibet. That worldwide dispersion allowed the differentiation of the group in several major lineages, the *Schlotheimiidae, Discamphiceratinae, Arietitidae* and *Lytocerataceae*, which were the roots of all other Jurassic and Cretaceous ammonites.

Acknowledgements

The study was supported by the Swiss National Science Foundation. JG thanks Oscar von Bischoffshausen, Cloudforest Expeditions, Arcenio Balcazar Saldana for their efficient logistic help in the field, Jose Machare, Victor Benavides and Silvia Rosas for their scientific support in Peru and Romain Minoia for his help in compiling the stratigraphic data from NW-Europe. We also thank Finn Surlyk for his editorial help and Mark Schmitz for his useful review of the initial manuscript.

Appendix A. Supplementary data

Supplementary data to this article can be found online at http://dx.doi.org/10.1016/j.palaeo.2012.04.030.

References

Bachmann, O., Charlier, B.L.A., Lowenstern, J.B., 2007. Zircon crystallization and recycling in the magma chamber of the rhyolitic Kos Plateau Tuff (Aegean arc). Geology 35, 73–76.
Bachmann, O., Schoene, B., Schnyder, C., Spikings, R., 2010. The $^{40}Ar/^{39}Ar$ and U/Pb dating of young rhyolites in the Kos-Nisyros volcanic complex, Eastern Aegean Arc, Greece: age discordance due to excess ^{40}Ar in biotite. Geochemistry, Geophysics and Geosystems 11, 1–14.
Bacon, C.R., Lowenstern, J.B., 2005. Late Pleistocene granodiorite source for recycled zircon and phenocrysts in rhyodacite lava at Crater Lake, Oregon. Earth and Planetary Science Letters 233, 277–293.
Bartolini, A., Guex, J., Spangenberg, J., Taylor, D., Schoene, B., Schaltegger, U., Atudorei, V., 2012. Disentangling the Hettangian carbon isotope record: implications for the aftermath of the end-Triassic mass extinction. Geochemistry, Geophysics and Geosystems 13, 1–11.
Bloos, G., Page, K., 2002. Global Stratotype Section and Point for base of the Sinemurian Stage (Lower Jurassic). Episodes 25, 22–28.
Cardenas, A.L., Harries, P.J., 2010. Effect of nutrient availability on marine origination rates throughout the Phanerozoic eon. Nature Geoscience 3, 430–434.
Charlier, B.L.A., Wilson, C.J.N., Lowenstern, J.B., Blake, S., Van Calstren, P.W., Davidson, J.P., 2005. Magma generation at a large hyperactive silicic volcano (Taupo, New Zealand) revealed by U–Th and U–Pb systematics in zircons. Journal of Petrology 46, 3–32.
Cirilli, S., Marzoli, A., Tanner, L., Bertrand, H., Buratti, N., Jourdan, F., Bellieni, G., Kontak, D., Renne, P.R., 2009. Latest Triassic onset of the Central Atlantic Magmatic Province (CAMP) volcanism in the Fundy Basin (Nova Scotia): new stratigraphic constraints. Earth and Planetary Science Letters 286, 514–525.
Clémence, M.E., Gardin, S., Bartolini, A., Paris, G., Beaumont, V., Guex, J., 2010. Benthoplanktonic evidence from the Austrian Alps for a decline in sea-surface carbonate production at the end of the Triassic. Swiss Journal of Geoscience 103, 293–315.
Cohen, A.S., Coe, A.L., 2007. The impact of the Central Atlantic Magmatic Province on climate and on the Sr- and Os-isotope evolution of seawater. Palaeogeography, Palaeoclimatology, Palaeoecology 244, 374–390.
Condon, D.J., McLean, N., Noble, S.R., Bowring, S.A., 2010. Isotopic composition ($^{238}U/^{235}U$) of some commonly used uranium reference materials. Geochimica et Cosmochimica Acta 74, 7127–7143.
Courtillot, V., Jaupart, C., Manighetti, I., Tapponnier, P., Besse, J., 1999. On causal links between flood basalts and continental breakup. Earth and Planetary Science Letters 166, 177–195.
Crowley, J.L., Schoene, B., Bowring, S.A., 2007. U–Pb dating of zircon in the Bishop Tuff at the millennial scale. Geology 35, 1123–1126.
Davydov, V.I., Crowley, J.L., Schmitz, M.D., Polatev, V.I., 2010. High-precision U–Pb zircon age calibration of the global Carboniferous time scale and Milankovitch band cyclicity in the Donets Basin, eastern Ukraine. Geochemistry, Geophysics and Geosystems 11, Q0AA04, http://dx.doi.org/10.1029/2009GC002736.
Erben, H.K., 1966. Über den Ursprung der Ammonoidea. Biological Review 41, 641–658.
Galli, M.T., Jadoul, F., Bernasconi, S.M., Cirilli, S., Weissert, H., 2007. Stratigraphy and palaeoenvironmental analysis of the Triassic–Jurassic transition in the western Southern Alps (Northern Italy). Palaeogeography, Palaeoclimatolology, Palaeoecology 244, 52–70.
Guex, J., 1991. Biochronological Correlations. Springer Verlag, Berlin.
Guex, J., 1995. Ammonites Hettangiennes de la Gabbs Valley Range. Mémoires de Géologie, Lausanne 27, 1–130.
Guex, J., 2003. A generalization of Cope's rule. Bulletin Société Géologique de France 174, 449–452.
Guex, J., 2006. Reinitialization of evolutionary clocks during sublethal environmental stress in some invertebrates. Earth and Planetary Sciences Letters 242, 240–253.
Guex, J., Davaud, E., 1984. The Unitary Associations method: use of graph theory and computer algorithm. Computers and Geosciences 10, 69–96.
Guex, J., Bartolini, A., Atudorei, V., Taylor, D., 2004. High-resolution ammonite and carbon isotope stratigraphy across the Triassic–Jurassic boundary at New York Canyon (Nevada). Earth and Planetary Science Letters 225, 29–41.
Haas, O., 1942. Recurrence of morphologic types and evolutionary cycles in Mesozoic ammonites. Journal of Paleontology 16, 643–650.
Hammer, O., Guex, J., Savary, J., 2011. The UAgraph program. folk.uio.no / ohammer / uagraph.
Hesselbo, S.P., Robinson, S.A., Surlyk, F., Piasecki, S., 2002. Terrestrial and marine extinction at the Triassic–Jurassic boundary synchronized with major carbon-cycle perturbation: a link to initiation of massive volcanism? Geology 30, 251–254.
Hyatt, A., 1889. Genesis of the Arietidae. Memoir Museum Comparative Zoology 16, 1–238.
Jablonski, D., 1996. Mass Extinctions: Persistent problems and new directions. In: G. Ryder, D. Fastovsky, and S. Gartner, eds., The Cretaceous-Tertiary Event and Other Catastrophes in Earth History(Snowbird III). Geological Society of America, Special Paper 307, 1–11.
Jones, C.J., Jenkyns, H.C., Coe, A.L., Hesselbo, S.P., 1994. Strontium isotopic variations in the Jurassic Cretaceous seawater. Geochimica Cosmochimica Acta 58, 3061–3074.
Kuiper, K.F., Deino, A., Hllgen, F.J., Krijgsman, W., Renne, P.R., Wijbrans, J.R., 2008. Synchronizing rocks clocks of Earth history. Science 320, 500–504.
Lucas, S.G., 1994. Triassic tetrapod extinctions and the compiled correlation effect. Canandian Society of Petroleum Geology, Memoir 17, 869875.
Mailliot, S., Mattioli, E., Guex, J., Pittet, B., 2006. The Early Toarcian anoxia, a synchronous event in the Western Tethys? An approach by quantitative biochronology (Unitary Associations), applied on calcareous nannofossils. Palaeogeography, Palaeoclimatology, Palaeoecology 240, 562–586.
Marzoli, A., Renne, P.R., Piccirillo, E.M., Ernesto, M., Bellieni, G., De Min, A., 1999. Extensive 200-million-year-old continental flood basalts of the Central Atlantic magmatic province. Science 284, 616–618.
Marzoli, A., Jourdan, F., Puffer, J.H., Cuppone, T., Tanner, L., Weems, R.E., Bertrand, H., Cirilli, S., Bellieni, G., De Min, A., 2011. Timing and duration of the Central Atlantic magmatic province in the Newark and Culpeper basins, eastern U.S.A. Lithos 122, 175–188.
Mattinson, J.M., 2005. Zircon U–Pb chemical abrasion ("CA-TIMS") method: combined annealing and multi-step partial dissolution analysis for improved precision and accuracy of zircon ages. Chemical Geology 200, 47–66.
McElwain, J.C., Wagner, P.J., Hesselbo, S.P., 2009. Fossil plant relative abundances indicate sudden loss of Late Triassic biodiversity in East Greenland. Science 324, 1554–1556.
McLean, N.M., Bowring, J.F., Bowring, S.A., 2011. An algorithm for U–Pb isotope dilution data reduction and uncertainty propagation. Geochemistry, Geophysics and Geosystems 12, Q0AA18, http://dx.doi.org/10.1029/2010GC003478.
Miller, J.S., Matzel, J.E.P., Miller, C.F., Burgess, S.D., Miller, R.B., 2007. Zircon growth and recycling during the assembly of large composite arc plutons. Journal of Volcanic Geothermermical Research 167, 282–299.
Min, K., Mundil, R., Renne, P.R., Ludwig, K.R., 2000. A test for systematic errors in $^{40}Ar/^{39}Ar$ geochronology through comparison with U/Pb analysis of a 1.1-Ga rhyolite. Geochimica et Cosmochimica Acta 64, 73–98.
Miskovic, A., Schaltegger, U., 2009. Crustal growth along a non-collisional cratonic margin: a Lu–Hf isotopic survey of the Eastern Cordilleran granitoids of Peru. Earth and Planetary Science Letters 279, 303–315.
Miskovic, A., Schaltegger, U., Spikings, R., Kosler, J., Chew, D.M., 2009. Tectono-magmatic evolution of Western Amazonia: geochemical characterization and zircon U–Pb

geochronologic constraints from the Peruvian Eastern Cordillera granitoids. Geological Society of America, Bulletin 121, 1298–1324.
Mundil, R., Ludwig, K.R., Metcalfe, I., Renne, P.R., 2004. Age and timing of the Permian mass extinctions: U/Pb dating of closed-system zircons. Science 305, 1760–1763.
O'Dogherty, L., Sandoval, J., Bartolini, A., Bill, M., Bruchez, S., Guex, J., 2006. Carbon-isotope stratigraphy and ammonite faunal turnover for the Middle Jurassic in the southern Iberian paleomargin. Palaeogeography, Palaeoclimatology, Palaeoecology 239, 311–333.
Ovtcharova, M., Bucher, H., Schaltegger, U., Galfetti, T., Brayard, A., Guex, J., 2006. New early to middle Triassic U–Pb ages from South China: calibration with the ammonoid biochronozones and implications for the timing of the Triassic biotic recovery. Earth and Planetary Science Letters 243, 463–475.
Pavlov, A.P., 1901. Le Crétacé inférieur de la Russie. Nouveaux Mémoires de la Société impériale des Naturalistes de Moscou 21, 1–87.
Ramezani, J., Schmitz, M.D., Davydov, V.I., Bowring, S.A., Snyder, W.S., Northrup, C.J., 2007. High-precision U–Pb zircon age constraints on the Carboniferous–Permian boundary in the southern Urals stratotype. Earth and Planetary Science Letters 256, 244–257.
Rosas, S., Fontboté, L., Tankard, A., 2007. Tectonic evolution and paleogeography of the Mesozoic Pucará Basin, central Peru. Journal of South American Earth Science 24, 1–24.
Ruhl, M., Deenen, M.H.L., Abels, H.A., Bonis, N.R., Krijgsman, W., Kürschner, W.M., 2010. Astronomical constraints on the duration of the early Jurassic Hettangian stage and recovery rates following the end-Triassic mass extinction (St Audrie's Bay/East Quantoxhead, UK). Earth and Planetary Science Letters 265, 262–276.
Schaltegger, U., Guex, J., Bartolini, A., Schoene, B., Ovtcharova, M., 2008. Precise U–Pb age constraints for end-Triassic mass extinction, its correlation to volcanism and Hettangian post-extinction recovery. Earth Planetary Science Letters 267, 266–275.
Schaltegger, U., Brack, P., Ovtcharova, M., Peytcheva, I., Schoene, B., Stracke, A., Bargossi, G., 2009. Zircon and titanite recording 1.5 million years of magma accretion, crystallization and initial cooling in a composite pluton (southern Adamello batholith, northern Italy). Earth Planetary Science Letters 286, 108–218.
Schindewolf, O.H., 1925. Entwurf einer Systematik der Perisphincten. Neues Jahrbuch für Mineralogie, Geologie und Paläontologie 52, 309–343.
Schindewolf, O.H., 1940. Konvergenzen bei Korallen und bei Ammoneen. Fortschritte Geologie Paläontologie 12, 387–491.
Schmitt, A.K., Stockli, D.F., Lindsay, J.M., Robertson, R., Lovera, O.M., Kislitsyn, R., 2010. Episodic growth and homogenization of plutonic roots in arc volcanoes from combined UTh and (UTh)/He zircon dating. Earth and Planetary Science Letters 295, 91–103.
Schmitt, A.K., Danišík, M., Evans, N.J., Siebel, W., Kiemele, E., Aydin, F., Harvey, J.C., 2011. Acigöl rhyolite field, Central Anatolia (part 1): high-resolution dating of eruption episodes and zircon growth rates. Contributions to Mineralogy and Petrology 162, 1215–1231.
Schmitz, M.D., Schoene, B., 2007. Derivation of isotope ratios, errors, and error correlations for U–Pb geochronology using Pb-205-U-235-(U-233)-spiked isotope dilution thermal ionization mass spectrometric data. Geochemistry, Geophysics and Geosystems 8, 1–20.
Schoene, B., Guex, J., Bartolini, A., Schaltegger, U., Blackburn, T., 2010a. Correlating the end-Triassic mass extinction and flood basalt volcanism at the 100,000-year level. Geology 38, 387–390.
Schoene, B., Schaltegger, U., Latkoczy, C., Günther, D., 2010b. A new method integrating high-precision U–Pb geochronology with zircon trace element analysis (U–Pb TIMS-TEA). Geochimica Cosmochimica Acta 74, 7144–7159.
Simon, J.I., Reid, M.R., 2005. The pace of rhyolite differentiation and storage in an 'archetypical' silicic magma system, Long Valley, California. Earth and Planetary Science Letters 235, 123–140.
Simon, J.I., Renne, P.R., Mundil, R., 2008. Implications of pre-eruptive magmatic histories of zircons for U–Pb geochronology of silicic extrusions. Earth and Planetary Science Letters 266, 182–194.
Sláma, J., Košler, J., Condon, D.J., Crowley, J.L., Gerdes, A., Hanchar, J.M., Horstwood, M.S.A., Morris, G.A., Nasdala, L., Norberg, N., Schaltegger, U., Schoene, B., Tubrett, M.N., Whitehouse, M.J., 2008. Plešovice zircon—a new natural reference material for U–Pb and Hf isotopic microanalysis. Chemical Geology 249, 1–35.
Spath, L.F., 1924. The ammonites of the Blue Lias. Proceedings of the Geological Association London 35, 186–211.
Tanner, L.H., Lucas, S.G., Chapman, M.G., 2004. Assessing the record and causes of late Triassic extinctions. Earth-Science Reviews 65, 103–139.
Tanner, L.H., Smith, D.L., Allan, A., 2007. Stomal response of swordfern to volcanogenic CO_2 and SO_2 from Kilauea volcano. Geophysical Research Letters 34, L15807, http://dx.doi.org/10.1029/2007 GL030320.
Taylor, D., Guex, J., 2002. The Triassic/Jurassic System boundary in the John Day Inlier, east-central Oregon. Oregon Geology 64, 3–28.
Ward, P.D., Haggart, J.W., Carter, E.S., Wilbur, D., Tipper, H.W., Evans, T., 2001. Sudden productivity collapse associated with the Triassic–Jurassic boundary mass extinction. Science 292, 1148–1151.
Whiteside, J.H., Olsen, P.E., Eglinton, T., Brookfieldd, M.E., Sambrotto, R.N., 2010. Compound-specific carbon isotopes from Earth's largest flood basalt eruptions directly linked to the end-Triassic mass extinction. http://dx.doi.org/10.1073/pnas.100170607.
Wilson, C.J.N., Charlier, B.L.A., 2009. Rapid rates of magma generation at contemporaneous magma systems, Taupo Volcano, New Zealand: insights from U–Th model-age spectra in zircons. Journal of Petrology 50, 875–907.